Article:
Lazareva, A, Owen, J orcid.org/0000-0003-0778-0858, Vargas, S et al. (2 more authors) (2021) Investigation of the evolution of an iron carbonate layer and its effect on localized corrosion of X65 carbon steel in CO2 corrosion environments. Corrosion Science, 192. 109849. ISSN 0010-938X

https://doi.org/10.1016/j.corsci.2021.109849

Investigation of the evolution of an iron carbonate layer and its effect on localized corrosion of X65 carbon steel in CO_2 corrosion environments

Anastasija Lazareva[a], Joshua Owen[a], Silvia Vargas[b], Richard Barker[a] and Anne Neville[a]

[a] *Institute of Functional Surfaces, School of Mechanical Engineering, University of Leeds, Leeds, LS2 9JT, United Kingdom*

[b] *BP America, Inc., Houston, Texas 77079*

Abstract

The general and localized corrosion of X65 carbon steel in CO_2-saturated environments conducive to iron carbonate ($FeCO_3$) formation has been studied using electrochemical measurements, together with post-test surface analysis. This research offers new insights into the evolution of $FeCO_3$ layer and its link to the subsequent initiation and propagation of localized corrosion. We identify crevice-like regions forming at boundaries/edges of the $FeCO_3$ crystals, which constitute the crystalline layer, where small cavities filled with electrolyte are restricted between developing crystals. It is apparent that such crevice-like features act as precursors to the localized/pitting corrosion on carbon steel over longer durations.

Key words: A. carbon steel; A. mild steel; B. SEM; B. XRD; C. crevice corrosion; C. pitting corrosion.

Introduction

While localized corrosion mechanisms of passive materials have become well established over past decades, the phenomenon of localized corrosion of active materials such as carbon steel in oilfield environments is still unclear. Since carbon and low-alloy steels remain the most common choices of material across a large spectrum of industries, it is crucial to understand the mechanism behind the initiation and propagation of localized attack, as well as study the role of corrosion products. In relation to carbon dioxide (CO_2) corrosion environments, iron carbonate ($FeCO_3$) layers are known to provide protection with regard to general corrosion. However, the effect of this layer on the initiation and propagation of localized attack in such environments remains undefined. The literature in the area of CO_2 corrosion of carbon steel is heavily focused towards uniform corrosion. Many models (mechanistic, empirical, and semi-empirical) for uniform corrosion exist and these all have varied levels of predictive capability across the spectrum of conditions that can be encountered across the energy sector [1, 2]. Localized corrosion remains one of the biggest threats to pipeline integrity, and unlike uniform corrosion, the fast initiation and propagation of pits is much harder to predict, detect and control. The complications in understanding localized corrosion and developing reliable predictive models lie in the small scale, rapid initiation and propagation of the attack and strong dependence on operating conditions, as well as potential transient changes in local solution chemistries.

Carbon and low-alloy steels remain a common choice of material across a broad range of industries due to their availability and ability to meet most of the project requirements. While carbon steel tends to perform very well in dry or low humidity environments, the integrity is likely to decrease dramatically in high humidity or aqueous systems, which leads to high corrosion rates. In oxygen-free environments, such as those encountered in typical oil and gas production, the presence of dissolved CO_2 can lead to appreciable general and localized corrosion [3].

Localized CO_2 corrosion remains one of the main reasons of premature failure of equipment in oil and gas operations [3]. Localized corrosion in the context of this work refers to any scenario where there are 'small' areas where the loss of metal thickness is many times greater than the average loss across the whole surface. In many instances, how this process initiates and propagates on carbon steel in many CO_2 environments still remains largely unknown, unlike the very well established differential aeration and discrete anode/cathode theories in the pitting of stainless steel [4, 5]. For pitting corrosion in carbon steel, it is still not understood whether the pit exists as an *entire* anode with the surrounding area (normally covered by a film) acting as a cathode. There is some evidence that suggests galvanic interactions have an influence on pitting corrosion in these conditions, but it is not determined whether a discrete anode/cathode set up is the only mechanism responsible for propagation [6, 7].

In a study by Huang [8, 9] the mechanism for localized under deposit corrosion in an inhibited environment was discussed in relation to silica sand deposition. Significant pitting corrosion was observed on the metal surface and attributed to the inability of the inhibitor to protect the steel in the crevices generated between each sand particle and the metal surface. Galvanic cells established between the inhibited steel surface and the local region under the sand particles promoted fast pit initiation and propagation, resulting in severe localized attack under the entire sand deposit [10]. It is plausible that similar crevice corrosion environments could be established between an inert $FeCO_3$ layer and a carbon steel surface.

Crevice corrosion can be described as a local attack of a secluded area on the metal surface where the access to the bulk electrolyte is restricted. The crevice corrosion phenomenon, like pitting, has been studied on passive materials across a wide range of systems, with several theories developed [11-14]. Pickering [12] proposed that the key parameter to understanding crevice corrosion is the IR drop (potential drop due to the solution resistance) or the variation in the potential between the crevice and the outer surface of the metal. It was also proposed that the potential shifting mechanism observed in the crevice could be a precursor for the breakdown of the passive film and subsequently, pit initiation. The effect of pH change inside of the crevice was discussed by Oldfield and Sutton [13], where a mathematical model was developed on the basis of critical crevice solution (CCS) to predict the drop in pH with time until a limiting or a critical value is reached. This drop in pH then results in the film breakdown and rapid localized corrosion. While this theory provides a basis to understand crevice corrosion on passive metals, the mechanism of crevice corrosion in active systems remains unclear.

Crevice corrosion of carbon and low-alloy steels has been discussed by several researchers. Wu et al. [15] observed higher rates of corrosion on a carbon steel surface exposed to a bulk electrolyte compared to a surface within a crevice. The term inverse crevice corrosion was introduced due to more aggressive corrosion being observed on a bare sample after galvanically coupling with a crevice sample. Wu et al. [15] proposed that carbon steel corrosion in a crevice involves many oxidation steps

that lead to metal dissolution and formation of different oxides. Therefore, the solution volume to surface area ratio and solution chemistry have a significant effect on crevice corrosion. Li et al. [16] studied crevice corrosion of carbon steel in CO_2-saturated environments in the presence of acetic acid (HAc). They reported that crevice corrosion of an N80 carbon steel surface was caused by the galvanic effect created by the different environments inside and outside of the crevice, with increasing concentrations of HAc in bulk solution stimulating crevice corrosion. Li et al. [16] showed that both the critical crevice solution theory (acidification) [13] and the IR drop theory [12] for passive materials could not explain the nature of crevice corrosion in carbon steel, mainly due to the non-passivating nature of the metal, as well as an observed increase in the pH inside of the crevice. It was found that the propagation of crevice corrosion on carbon steels is attributed to a more negative potential inside of the crevice, which makes it a net anode, compared to the potential outside of the crevice, which becomes a cathode [16].

The work presented in this paper is focused exclusively towards understanding the role of $FeCO_3$ accumulation on carbon steel surfaces and their potential link with the initiation and/or propagation of localized attack. Such layers establish themselves on carbon steel when the product of the local activities of Fe^{2+} and CO_3^{2-} ions at the surface exceed the solubility product, resulting in precipitation [17]:

$$Fe^{2+} + CO_3^{2-} \rightarrow FeCO_{3(s)} \quad (1)$$

$FeCO_3$ has been extensively studied by several researchers, including discussion of their kinetics and formation characteristics [17-23], galvanic effects and influence on pseudo-passivation behavior [6, 7, 24], as well as localized CO_2 corrosion in presence of such films [25-27]. However, a detailed discussion in relation to the mechanism of localized corrosion has not been provided. While there are theories with regard to protective properties of $FeCO_3$, the local interaction between the corrosion product and the metal surface is yet to be fully characterized.

Pit propagation under the $FeCO_3$ layer was reported by Pessu et al. [26], and was attributed to small cavities within $FeCO_3$ layer at the interface. In addition, pseudo-passivation was found to be one factor clearly related to pit initiation and propagation, with pits in excess of 30 µm deep being recorded soon after a sudden increase in Open Circuit Potential (OCP). Nevertheless, mechanical and/or chemical removal of the $FeCO_3$ layer is believed to be the main reason for localized corrosion of carbon steel, driven by the galvanic interactions between the local bare metal surface and the significantly larger areas of metal surface covered by the corrosion product [25, 28, 29]. However, the question arises as to whether localized corrosion, with similar mechanisms to crevice corrosion attack, occurs at the metal surface *underneath* a densely covered layer without any macroscopic damage to the $FeCO_3$ layer. In this present study, general and localized corrosion under the $FeCO_3$ layer on X65 carbon steel in 3.5 wt.% sodium chloride (NaCl) CO_2-saturated environment is analyzed using electrochemical techniques, scanning electron microscopy (SEM) and 3D surface analysis. The extent of corrosion is quantified (both localized and general) as a function of different stages of the $FeCO_3$ growth process.

Experimental

Experimental Setup and Material Preparation

X65 carbon steel test specimens were used as the working electrodes in a three-electrode cell configuration. The chemical composition of the X65 carbon steel used is provided in Table 1. Wires

were soldered to the reverse face of the samples before being embedded in a non-conducting resin, with an exposed surface area of 4.9 cm^2 to 1 L of solution. Prior to the start of each experiment, the surface of the electrode was wet-ground with silicon carbide paper up to 600-grit, degreased with acetone, rinsed with distilled water and dried with compressed air before being placed in the test solution.

Table 1. X65 carbon nominal composition (wt.%). Fe to balance

C	Si	Mn	P	S	Cr	Mo	Cu	Al	Ti	V	B	N
0.10 - 0.14	0.15-0.25	1.25 - 14	<0.025	<0.003	0.15	0.15 - 0.20	<0.20	0.015 - 0.025	<0.05	0.05 - 0.07	<0.0005	<0.015

It is widely reported in literature, that at higher pH (pH>6) and higher temperature (T>60°C) [20], precipitation of a $FeCO_3$ layer proceeds rapidly and results in a densely packed and protective corrosion product. Hence, all experiments were conducted in 3.5 wt.% NaCl 1 L solutions at 80°C and pH 6.8. Prior to each experiment the test solution was saturated with CO_2 gas for a minimum of 12 h at room temperature. Sodium bicarbonate was then used to increase the pH of the bulk solution to 6.8 after heating to the desired test temperature. All tests were carried out at atmospheric pressure. A standard three electrode bubble cell (Figure 1) was used in order to conduct CO_2 corrosion experiments with X65 carbon steel serving as the working electrode, a silver/silver chloride (Ag/AgCl) reference electrode and a platinum counter electrode. Table 2 summarizes the test conditions for the experimental work carried out in this paper. All experiments were repeated at least twice to ensure reproducibility.

Table 2. Experimental test matrix for the 9, 22 and 43 h immersion tests.

Parameter	Value
Material	API 5L X65 carbon steel 4.9 cm^2 exposed surface
Test Brine	Distilled water, 3.5 wt.% NaCl
Bulk pH	6.8, adjusted using $NaHCO_3$
Temperature	80°C
Immersion time	9, 22 and 43 hours

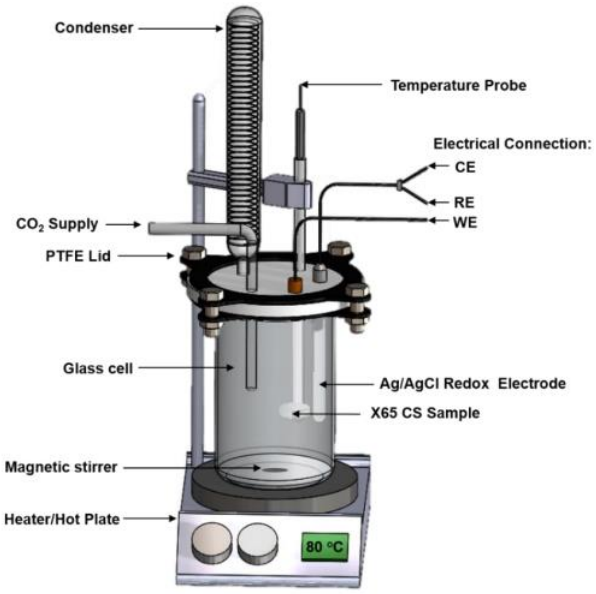

Figure 1. A schematic of the three-electrode cell and the bubble cell setup used for immersion experiments.

Electrochemical measurements were conducted using an ACM Gill 4 potentiostat. Electrochemical Impedance Spectroscopy (EIS) measurements were performed by applying ±10 mV perturbation about the OCP with a range of frequency from 30 kHz to 0.01 Hz every 1 hour. Ten measurements were taken per frequency decade and the OCP was monitored in between each EIS measurements. The obtained R_{ct} values were used to calculate the corrosion rate. The fitting of the impedance data was performed using ZView software.

According to the Stern-Geary Equation [30], R_{ct} is inversely proportional to instantaneous corrosion rate and can be related to the corrosion current density (i_{corr}) by:

$$R_{ct} = \frac{\Delta E}{\Delta i_{\Delta E \to 0}} = \frac{B}{i_{corr}} = \frac{\beta_a \beta_c}{2.303 i_{corr}(\beta_a + \beta_c)} \quad (2)$$

Rearranging gives:

$$i_{corr} = \frac{\beta_a \beta_c}{2.303 R_{ct}(\beta_a + \beta_c)} \quad (3)$$

where R_{ct} is the charge transfer resistance ($\Omega.cm^2$), i_{corr} is the corrosion current density (A/cm^2) and B is the proportionality constant known as the Stern-Geary coefficient (V) which is determined by anodic (β_a) and cathodic (β_c) Tafel slopes (V).

For the corrosion rate calculations, the anodic Tafel slope (β_a) value was set at 0.06 V, as measured and performed previously in the study by Burkle et al. [31] under the same experimental conditions. The cathodic Tafel slope (β_c) was set at 0.12 V, a commonly accepted value for CO_2 systems characterized by Nesic et al. [32]. Therefore, the Stern-Geary coefficient B was maintained at 0.017 V. Using the value of i_{corr} obtained in Equation (3), the corrosion rate (CR) in mm/year was obtained through the following Equation (4) based on the Faraday's Law:

$$V_c = K \frac{i_{corr} M_{Fe}}{nF\rho} \quad (4)$$

Where K is a conversion factor to obtain V_c in mm/year (K = $3.16x10^8$) i_{corr} is the corrosion current density (A/cm^2), M_{Fe} is the atomic weight of Fe (55.85 g/mol), n is the number of electrons exchanged ($2e^-$), F is the Faraday constant (96485 C/mol) and ρ is the density of Fe (7.88 g/cm^3).

Post Experimental Surface Analysis

To assess the coverage and the morphology of the corrosion layer, SEM images were collected using a Hitachi TM3030 Benchtop SEM. Micrographs were acquired using the accelerating voltage of 15 kV via the Secondary Electron (SE) mode. Surface coverage and size distribution was assessed using ImageJ software based on the differences in contrast of the crystals against the steel surface of the binary images. Depending on the noise and the quality of the image, chosen thresholds were applied to enhance the contract between the $FeCO_3$ crystals and the steel surface. Filtered objects, in this instance $FeCO_3$ crystals, were then measured to obtain diameter and surface coverage.

X-Ray diffraction (XRD) patterns for each sample were obtained using a Siemens Bruker D8 Advance multipurpose diffractometer by employing 40 kV ($K\alpha_{1+2}$) Cu radiation over a scattering angle range of $20°<2\Theta<70°$. The step size was 0.033 per second and took approximately 50 minutes per scan.

Corrosion products were subsequently removed in accordance with ASTM Standard G1-03(2017) [33] by gently wiping the surface with a cotton pad soaked in Clarke's solution (20g antimony trioxide (Sb_2O_3)+ 50 g stannous chloride ($SnCl_2$) + 1,000 ml 38% hydrochloric acid (HCl)), before rinsing the sample with distilled water, followed by ethanol and drying with compressed air. SEM and surface profilometry were performed on samples after corrosion product removal.

A 3D non-contact surface profilometer (BRUKER NPFLEX™) was used to evaluate the damage to X65 mild steel caused by localized corrosion. A 1x1 mm^2 area in the center of each sample was scanned. Raw data was analyzed and filtered in the Vision64 software by applying carefully chosen thresholds, to determine pit depths and diameters.

X65 carbon steel samples were etched for microstructural analysis using 3% Nital solution in accordance with ASTM E407 - 07(2015) [34]. Carbon steel samples were placed into the solution for 5-10 seconds, rinsed with distilled water and analyzed under an optical microscope to reveal the microstructure.

Results

Electrochemical measurements coupled with surface analysis

To understand the effect of the $FeCO_3$ evolution on the corrosion behavior of X65 carbon steel, EIS measurements were performed. Figure 2 shows the changes in the EIS spectra throughout the duration of the experiment. The Nyquist plots initially show a single time constant represented by a semicircle with an increasing diameter over time at the early stages of the experiment. A formation of a second semi-circle was observed at later stages of the experiment at lower frequency (LF), with the diameter of both semicircles increasing with time. Based on the data obtained from the Nyquist plots, two Electrochemical Equivalent Circuits (EEC) were built to understand the changes in impedance behavior. Figure 3 shows both EEC at the early stages of the experiment, as well as at the later stages of the experiment where $FeCO_3$ layer can be found on the surface.

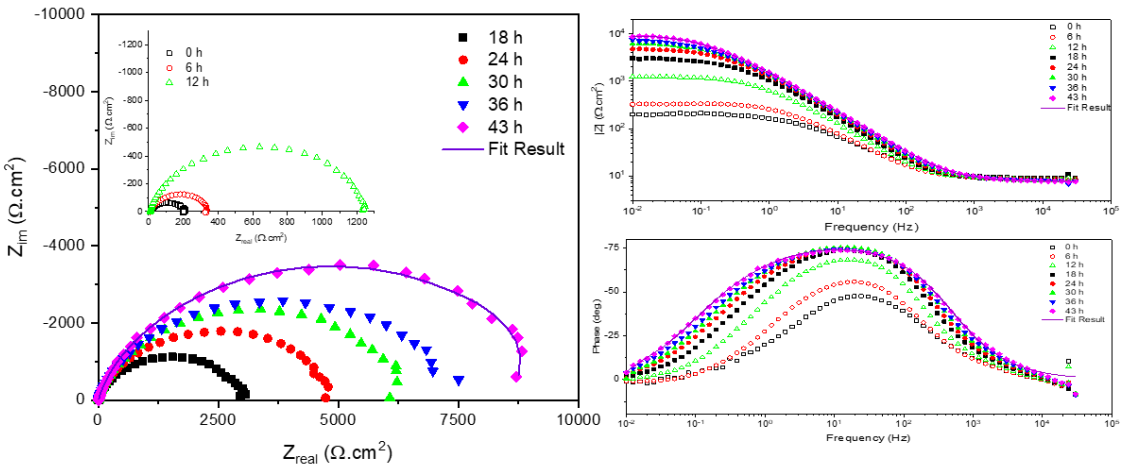

Figure 2. Nyquist plot and corresponding Bode plots of X65 carbon steel in CO_2-saturated environment at 80°C, pH 6.8, 3.5 wt.% NaCl.

Figure 3(a) shows a standard Randles EEC model which is commonly used to characterize a corroding metal interface without a corrosion product layer. Figure 3(b) shows a more complex EEC diagram showing the impedance of $FeCO_3$ layer in the high frequency region represented through R_{pore} and C_{FeCO_3}. The mass transfer barrier is represented through the R_{ct} and Warburg semi-infinite element (W) in the low frequency region. Both of the EEC are in agreement with the literature [35, 36], and the fit results are shown in Figure 2.

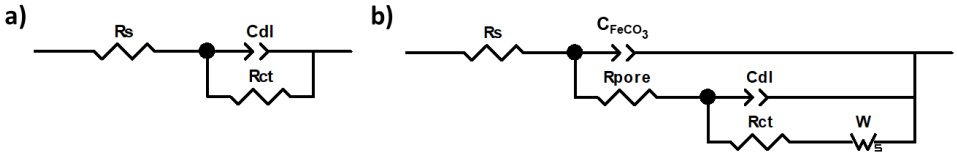

Figure 3. Equivalent electrical circuit a) at the start of the experiment, and b) after the precipitation of the $FeCO_3$ layer on the X65 carbon steel surface. R_s- solution resistance in $\Omega.cm^2$, C_{dl}- Constant Phase Element (CPE) double layer capacity parameter in $\mu F.cm^{-2}$, R_{ct}- charge transfer resistance in $\Omega.cm^2$, C_{FeCO_3} - CPE film parameter in $\mu F.cm^{-2}$, R_{pore} – pore resistance in $\Omega.cm^2$ and W- Warburg semi-infinite element.

The values of the parameters used to fit EEC and calculated active surface value (S_a) are shown in Table 3. Active surface area can be calculated from the ratio of the double layer capacitance at the start of the experiment ($C_{dl}(0)$) and at any given time ($C_{dl}(t)$) [35]:

$$S_a\%(t) = \frac{C_{dl}(t)}{C_{dl}(0)} \times 100 \quad (5)$$

Precipitation of $FeCO_3$ on the metal surface is known to reduce the general corrosion rate of the metal by reducing the active surface area. Charge transfer resistance is known to be inversely proportional to the corrosion rate, and hence the active surface S_a. As $FeCO_3$ layer evolves on the surface, the active surface area decreases, leading to an increase in charge transfer resistance as observed in Table 3. It was found that less than 50% of the surface was active after 18 hours of exposure, reducing further to 33% after 42 hours of the experiment. An initial increase in active surface might be explained by the roughening of the metal surface due to general corrosion [35]. The increase in pore resistance

(R_{pore}) with time indicates the decrease in pore diameter, or possibly, an increase in pore length as $FeCO_3$ layer continues to evolve [35].

Table 3. EIS fitting results and calculated value of S_a.

Time h	R_s $\Omega.cm^2$	C_{dl} $\mu F.cm^{-2}$	R_{ct} $\Omega.cm^2$	C_{FeCO_3} $\mu F.cm^{-2}$	R_{pore} $\Omega.cm^2$	Chi-squared	S_a %
0	8.9	594	198	-	-	0.006	100.0
6	8.6	437	119	351	210	0.004	73.7
12	8.5	669	358	201	875	0.003	112.7
18	8.5	291	1522	134	1543	0.007	49.0
24	8.2	263	2316	120	2569	0.002	44.4
30	8.1	252	2975	113	3503	0.002	42.4
36	7.9	260	3234	124	4082	0.003	43.7
42	7.8	195	4315	118	5025	0.002	32.8

The evolution of the $FeCO_3$ layer was investigated in a CO_2-saturated environment at 80°C, pH 6.8, at atmospheric pressure and 3.5 wt.% NaCl solution. The corrosion rate and OCP were monitored with respect to time as shown in Figure 4. From Equation (3) and (4), R_{ct} is known to be inversely proportional to the corrosion rate. An initial increase in corrosion rate within the first 6 hours indicates that the metal surface is actively corroding, followed by a progressive decrease over a period of over 37 hours, which coincides with the changes in charge transfer resistance and the double layer capacitance with time. The gradual decrease in corrosion rate, which is widely reported in the literature, is attributed to formation of a protective layer, meaning in this instance that the conditions are favorable for the nucleation and growth of $FeCO_3$ crystals on the steel surface. The reduction of the active surface and in turn, the double layer capacity, is due to the blocking effect of the surface caused by the evolving $FeCO_3$ layer.

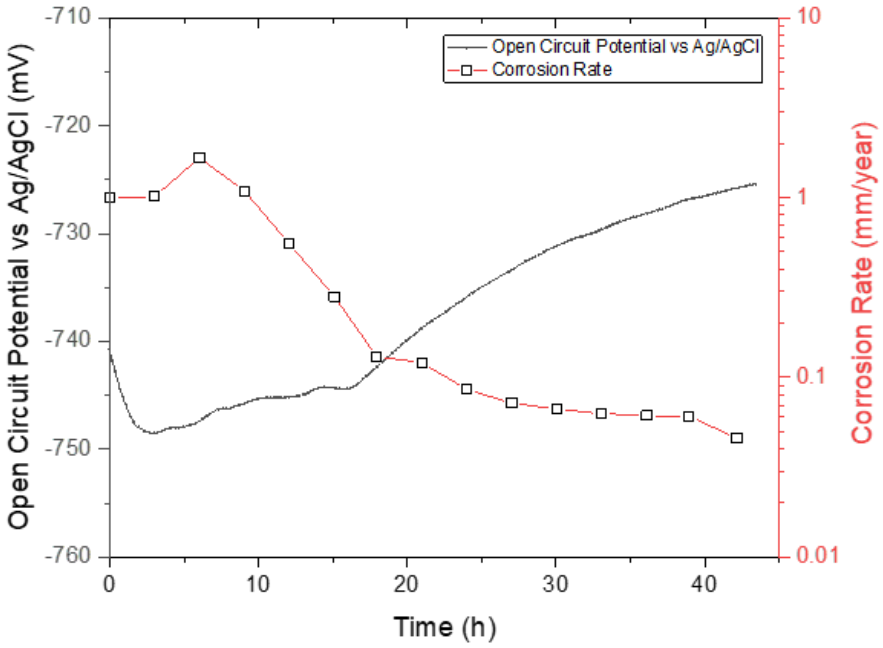

Figure 4. Change in corrosion rate obtained from EIS and Open Circuit Potential vs Ag/AgCl of X65 carbon steel with time.

SEM images of the $FeCO_3$ crystals are shown in Figure 5(a, c, e). As expected, the decrease in corrosion rate can be associated with $FeCO_3$ accumulation on the steel surface. Immersion tests were performed for 9, 22 and 43 hours. Corrosion rates reach a peak value of 1.66 mm/year after 6 hours of immersion, followed by a decrease in corrosion rate to 1.09 mm/year and 0.10 mm/year after 9 and 22 hours of immersion, respectively. At 24 hours the corrosion rate falls below 0.1 mm/year which is close to the steady state corrosion rate observed in many previous studies considering the protective properties of $FeCO_3$ [22, 26, 37]. The corrosion rate continues to steadily decrease throughout the course of the experiment, with a final value of 0.05 mm/year after 43 hours of immersion. Partial coverage of X65 carbon steel with $FeCO_3$ is achieved after 9 hours and 22 hours as shown in Figure 5(a) and (c). From SEM images, the coverage by $FeCO_3$ crystals remains partial after 22 hours, they appear visibly larger in size and cover approximately 51% of the metal surface, in contrast to 42% coverage after 9 hours. After 43 hours of immersion, near full coverage (99%) of the metal surface is achieved, as shown in Figure 5(e). While the calculated active surface from the impedance data indicates that 50% of the surface is active after 22 hours of immersion, which is in agreement with the estimated surface coverage from the SEM images, the values of the active surface at the end of the experiment vary significantly. It was estimated that 99% of the surface is covered after 43 hours of immersion, however the active surface calculations based on the impedance data show that at least 32% of the surface remains active after 43 hours of the immersion testing. The estimation of surface coverage from the top view of the SEM images is not entirely representative of the true active surface area, whereas the active surface estimation derived from the impedance measurements corresponds more accurately with the profilometry data in Figure 6(d), accounting for any void or areas where $FeCO_3$ layer is not in direct contact with the metal surface. Referring to XRD patterns shown in Figure 5(b, d, f), the only identifiable crystalline compound was found to be $FeCO_3$. The SEM results in Figure 5(a) show a mixture of plate-like and prismatic shaped crystals on the metal surface after 9 hours of exposure. Although not detected on the XRD patterns in Figure 5(b), the plate-like crystals closely resemble chukanovite ($Fe(OH)_2CO_3$), which is believed to be an intermediate metastable specie, which with time, transforms into $FeCO_3$ [38, 39].

The average sizes of the $FeCO_3$ crystals after 9, 22 and 43 hours of immersion were found to be 29.1±0.3 µm, 39.4±1.7 µm and 25.4±0.9 µm, respectively. The SEM images of X65 carbon steel after 22 and 43 hours of immersion showed no chukanovite on the metal surface.

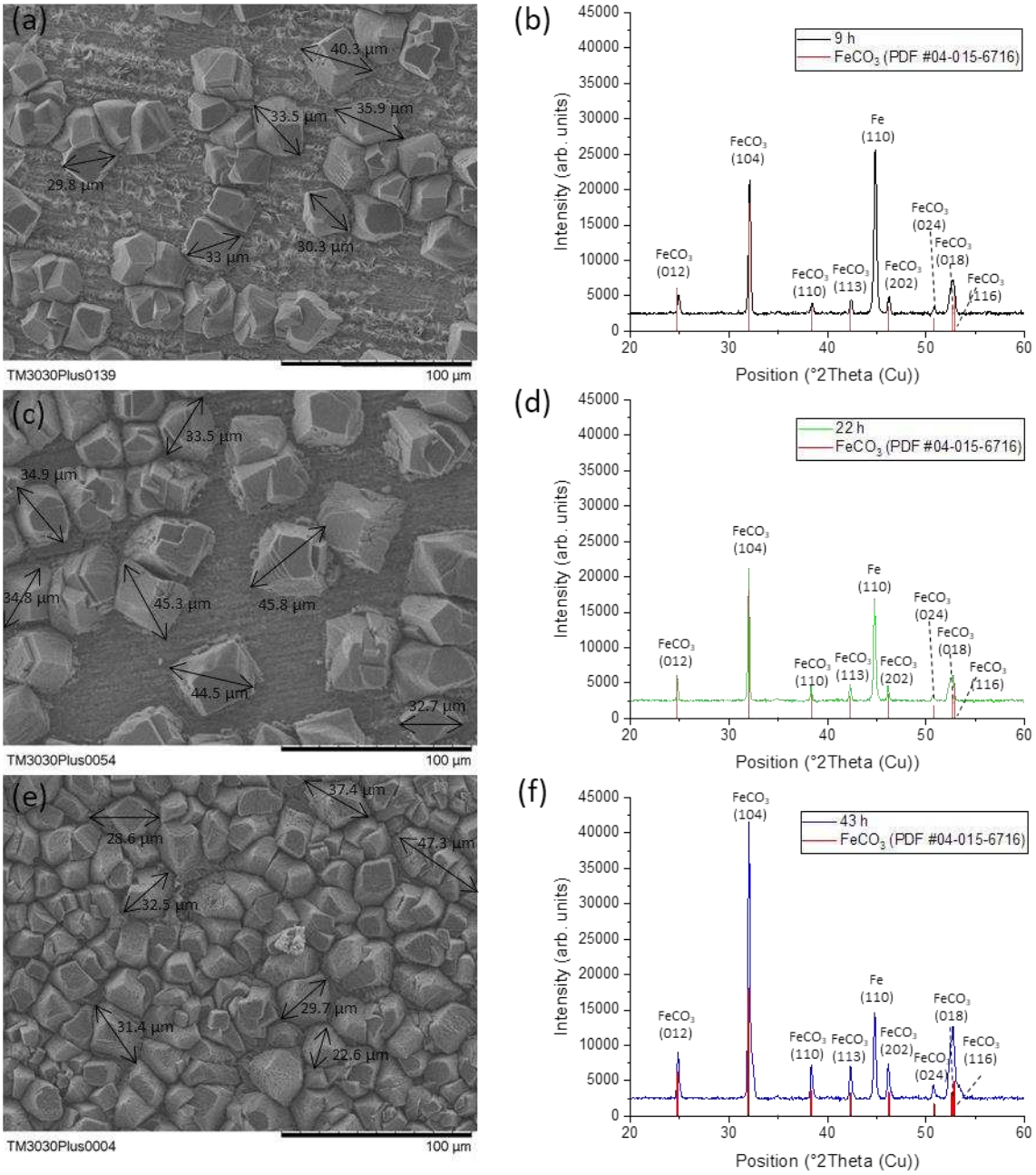

Figure 5. SEM images (a, c, e) and corresponding XRD patterns (b, d, f) after 9, 22 and 43 hours of immersion tests. ICDD $FeCO_3$ PDF #04-015-6716.

Figures 6(a, b) shows SEM images of the X65 metal surface after corrosion product removal with Clarke's solution. Interestingly, it appears that at very early stages of $FeCO_3$ evolution, when general corrosion rate values remain high, imprints of the crystals can be seen on the surface of the metal after the removal of $FeCO_3$, averaging at 29.8±2.3µm. Grinding marks are also visible under the preserved metal surface together with small crevice-like features (Figure 6(a, b)). As the $FeCO_3$ layer progresses to dominate the surface, the imprints become deeper and more distinct, as can be seen from a 2D surface scan and the profile in Figure 6(d, e), averaging at 35.7±2.44 µm in size. The ferritic/pearlitic microstructure of X65 carbon steel is shown in Figure 6(c). The imprints on the metal surface closely resemble the size of the $FeCO_3$ crystals and appear to have no link to the microstructure

of X65 carbon steel, which is considerably smaller (average grain size of ferrite was found to be 15.2±0.5 µm), as shown in Figure 6 (c). This suggests the process is not dominated by intergranular corrosion. Furthermore, it is historically known that steel microstructure has a contrasting influence on corrosion behavior and formation of a protective $FeCO_3$ layer. The revealing of Fe_3C can support the formation of a protective and adherent $FeCO_3$ layer, but it is also known to facilitate micro-galvanic cell formation on the metal surface, resulting in selective attack at and around pearlite grains [3, 40-42].

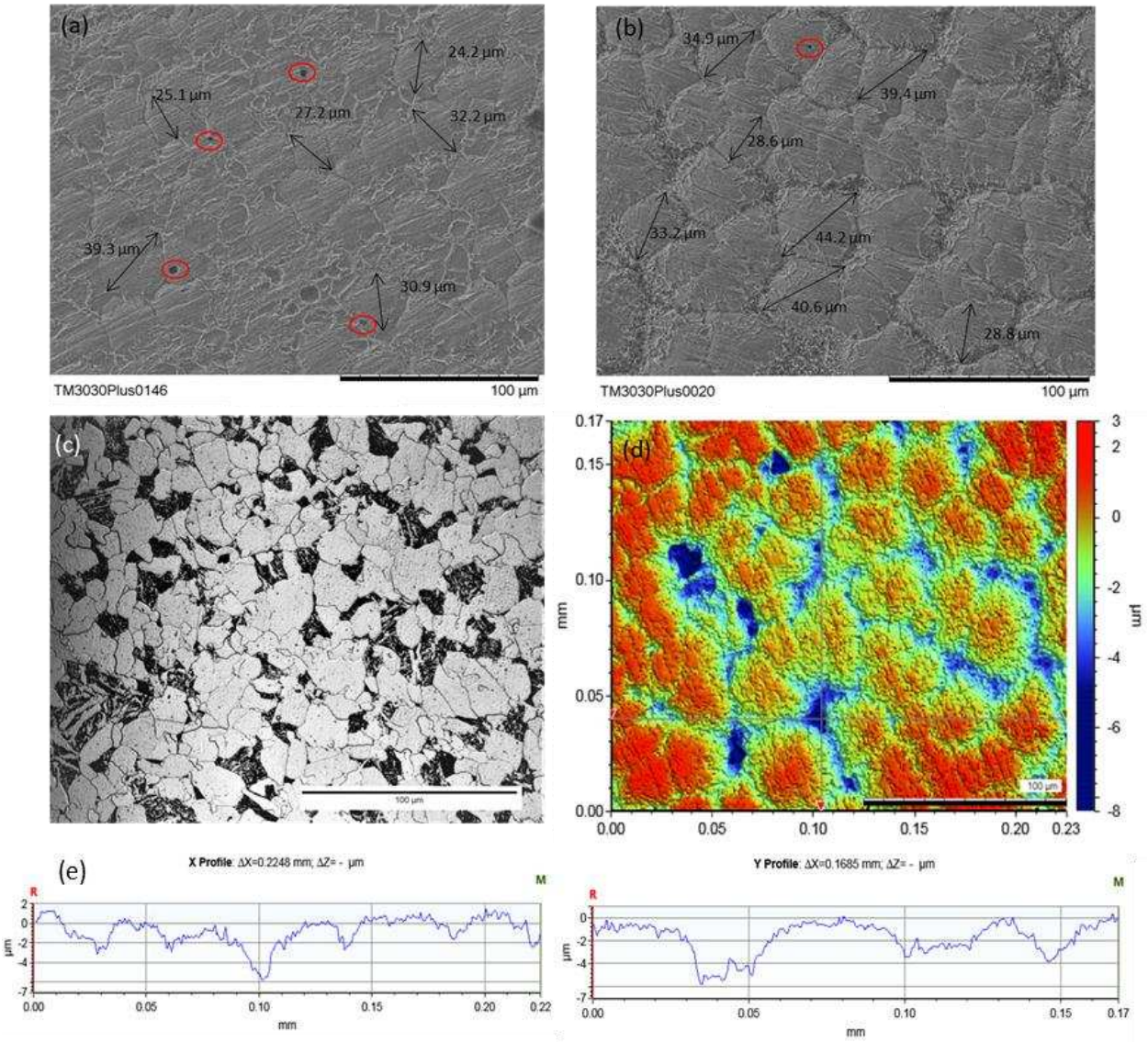

Figure 6. (a) and (b) represent SEM images of X65 carbon steel samples after corrosion product removal, after 9 hours and 43 hours of immersion respectively, with footprints of the crystals together with crevice-like geometries (red circles) visible on the metal surface; (c) represents the microstructure of X65 carbon steel and (d) shows surface profilometry image of the same sample after 43 hours of immersion and (e) provides X and Y cross section profiles of the surface depicted in (d).

3D surface characterization of X65 carbon steel samples after the $FeCO_3$ removal was performed using a Bruker NPFLEX™ 3D optical microscope. Corrosion damage to the surface existed in the form of small trenches and pits. The results suggest that as the film evolves and the general corrosion rate

decreases, the average diameter and the depth of pits increase, as shown in Table 4. A 2D pit morphology profile and a 3D surface profile are shown in Figure 7.

Table 4. Average diameter and the depth of pits for different corrosion rate values.

Experiment	*Average diameter, µm	*Average depth, µm
9 hours	8.4 ± 1.4	3.2 ± 0.4
22 hours	27.8 ± 6.7	5.6 ± 0.9
43 hours	37.0 ± 5.2	8.5 ± 0.2
*** Average of the ten deepest pits**		

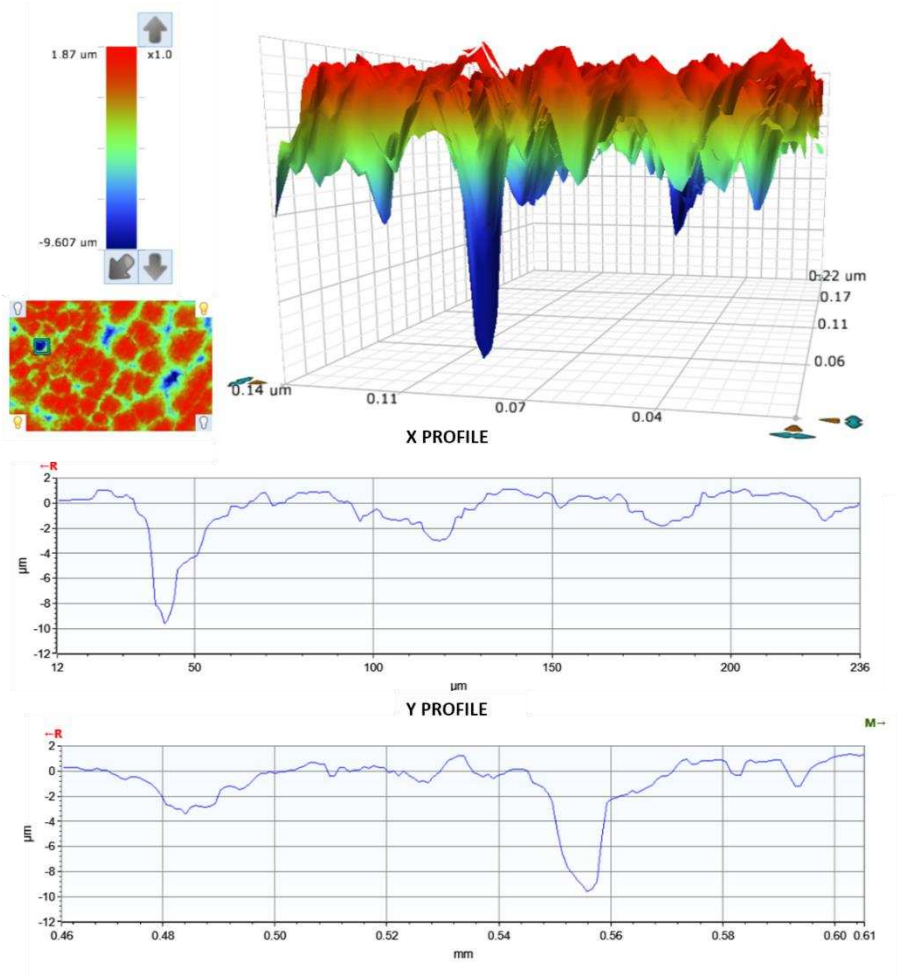

Figure 7. 2D and 3D pit morphologies of a deepest pit of a sample with general corrosion rate below 0.1 mm/year.

Discussion

It is believed that the cause of the localized corrosion in the presence of the $FeCO_3$ layer is either due to mechanical and/or chemical dissolution of the film. However, in the present study, even though no mechanical and/or chemical dissolution of $FeCO_3$ layer occurred, X65 carbon steel suffered localized corrosion attack with the presence of the developing and intact, protective $FeCO_3$ layer.

The evolution of the $FeCO_3$ layer was assessed with regard to the change in general corrosion rate values. OCP and corrosion rate were measured as a function of time as shown in Figure 4. As the corrosion rate drop is often associated with the $FeCO_3$ precipitation, $FeCO_3$ layer evolution was analyzed and aligned to the reduction in general corrosion rate. From the SEM images presented in Figure 5, it is evident that as the corrosion rate decreases, the $FeCO_3$ crystals increase in size and spread across the X65 carbon steel surface, eventually covering the majority of the metal surface after 43 hours of immersion. The diffusion barrier and/or the surface blocking effect offered by the $FeCO_3$ layer reduces the general corrosion rate below 0.1 mm/year after 24 hours of testing, as can be seen in Figure 4. XRD patterns shown in Figure 5 illustrate the change in $FeCO_3$ content at early stages of $FeCO_3$ precipitation (Fig. 5(b)) and when the surface is covered with the $FeCO_3$ layer (Fig. 6(f)). XRD patterns show that there is an increase in major $FeCO_3$ peak intensity ($FeCO_3$ (104) plane at 2θ = ~32°) and significant decrease in a major Fe peak intensity (Fe (110) plane at 2θ = ~45°) over time.

Micrographs of X65 carbon steel surface after corrosion product removal in Figure 6 show preferential corrosion around $FeCO_3$ crystal boundaries and small crevices at the boundaries of the crystals. As shown in Figure 6(a, b), the locations where the $FeCO_3$ crystals form show preserved metal surface underneath, with polishing marks still visible. The pattern underneath is more associated with $FeCO_3$ crystals, rather than the microstructure of X65 steel presented in Figure 6(c), however there is a likelihood that the two parameters are dependent on each other. Small crevice-like geometries were found to develop at very early stages of $FeCO_3$ growth, directly under or at the boundaries of the crystals. Upon further examination, it was found that the steel suffered localized attack in the form of narrow pits reaching a maximum depth of 8.5 μm after 43 hours of immersion. The data presented in Table 4 suggests that as the $FeCO_3$ layer evolves on the metal surface, so too does the extent of localized corrosion, initiating in the form of small shallow crevices and propagating further under the $FeCO_3$ crystals in a form of deeper narrow pits.

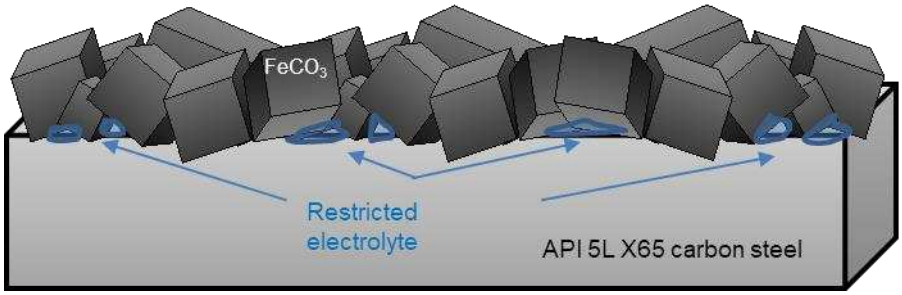

Figure 8. A schematic illustration of $FeCO_3$ layer on X65 carbon steel surface with electrolyte trapped beneath $FeCO_3$ crystals.

Due to the surface finish of the metal and the heterogeneity of the $FeCO_3$ layer, small pockets of electrolyte are likely to be restricted in between the fast forming $FeCO_3$ crystals (in favorable conditions [20]) or directly under individual crystals, as proposed in Figure 8. Crevices were found directly under individual $FeCO_3$ crystals at early stages of the $FeCO_3$ layer evolution as shown in Figure 6(a). It appears, that crevices initiate as the first $FeCO_3$ crystals form on the metal surface. The following scenario for the initiation of the localized corrosion can be proposed:

The initial corrosion is driven by the dissolution of ferrite and consequent exposure of Fe_3C to the solution. The establishment of the micro-galvanic cell between more cathodic Fe_3C and ferrite would promote corrosion on the metal surface. Subsequently, exposed Fe_3C would facilitate the formation of $FeCO_3$ crystals, which would lead to a decrease in the corrosion rate, as seen in Figure 4 [3, 42].

A galvanic driving force would initiate as a result of the differences between the electrolyte chemistry under individual $FeCO_3$ crystals and the bulk solution chemistry due to the $FeCO_3$ layer acting as a physical diffusion barrier for corrosive species. The change is species in the crevice is likely to lead to a potential difference between a small area under the $FeCO_3$ crystal (crevice) and the significantly larger bare metal surface. A micro-galvanic cell is then established on the same metal samples, making the area under the crystal an anode, and the exposed metal surface a cathode. Such a hypothesis is in agreement with the literature on the crevice corrosion of active materials. Li et al. [16] reported that the galvanic interactions between the electrode inside of the crevice (anode) and outside of the crevice (cathode) are responsible for the crevice corrosion of N80 carbon steel. In addition, the pH inside of the crevice increased, ruling out the possibility of the acidification theory, a common cause of localized corrosion on passive materials. Similarly, in an investigation of the crevice corrosion of X52 carbon steel, an increase in the corrosion rate of the electrode in the crevice solution, compared to the electrode exposed to bulk solution was reported [43]. The enhanced corrosion of the crevice electrode was attributed to the change in the potential between the small anode (electrode in the crevice solution) and a larger cathode (electrode in bulk solution), which led to the establishment of the galvanic corrosion cell. Likewise, no acidification inside of the crevice took place, and crevice solution pH was found to increase with time [43]. Although most of the crevice corrosion testing is done on a macroscopic scale, i.e. coupling of electrodes, it is suggested that the findings can be transferred to a smaller, microscopic scale, where the galvanic cell is established on the same metal sample, as suggested in this paper.

The manner in which crevice-like features initiate under the individual $FeCO_3$ crystals can be compared to the initiation and propagation of localized attack in under deposit corrosion environments. Similarly to $FeCO_3$ layers, silica sand deposits act as an inert diffusion barrier, limiting the mass-transfer of corrosive species to and away from the metal surface. The pH values under such deposits can reach values of 1-2 units higher, compared to those of bulk pH [10]. It was found that the diameter of the crevice was identical to the diameter of the silica sand particle. Consequently, the pit initiates underneath, exactly at the center of the crevice [8-10]. The above findings closely resemble the growth pattern in the present study. From Table 4, it is evident that the crevice continued to grow both laterally and in depth throughout the duration of the experiment, reaching an average diameter of 37 μm, whereas the average diameter of the crystal imprints on the surface was found to be 35.7 μm.

The driving force for the propagation of localized corrosion under a fully formed protective $FeCO_3$ still remains unknown. It is commonly accepted that a protective $FeCO_3$ layer acts as a diffusion barrier, offering excellent corrosion protection in terms of uniform corrosion. However, local loss of the $FeCO_3$ layer is possible, either due to chemical/mechanical removal of the film, or partially protective properties of $FeCO_3$ layer. The area under the $FeCO_3$ layer is believed to have a higher potential, hence it acts as a cathode when coupled with a bare metal surface, which acts as an anode. The established galvanic cell will result in the bare metal surface being polarized anodically, in turn accelerating localized corrosion of the metal. Although a protective film is formed in the experiments performed in this paper, the metal evidently suffered from localized corrosion without any chemical/mechanical dissolution of the film. If no mass-transfer of the corrosive species between the bulk solution and the crevice takes place, then the separation of anodes and cathodes within the crevice could be responsible for the propagation of localized corrosion. Such local galvanic cells can develop as a result of differences in local chemistry due to the heterogeneity of the $FeCO_3$ layer and, possibly, due to geometrical configuration of the crevice [44].

Conclusions

The evolution of the $FeCO_3$ layer on X65 carbon steel in CO_2-saturated environments was analyzed and the effect of the layer on localized corrosion was discussed. The following conclusions can be drawn:

- Localized corrosion manifest itself when the $FeCO_3$ layer starts dominating the surface; early signs of localized corrosion in a form of crevices were found at early stages of $FeCO_3$ evolution.
- Preferential corrosion on the steel surface resembling the 'footprint' of $FeCO_3$ crystals was observed after the removal of the corrosion product, leaving imprints of preserved metal on X65 carbon steel. The imprint pattern is attributed to the $FeCO_3$ crystals rather than the microstructure of the metal.
- Localized corrosion does is not solely attributed to the local breakdown of the film, as pits and crevices were found under densely packed $FeCO_3$ crystals. In turn, the inhomogeneity of the $FeCO_3$ layer is believed to be the cause of localized corrosion.
- A mechanism responsible for the initiation and propagation of localized corrosion on X65 carbon steel surface was proposed. It is believed that the crevice corrosion initiates under individual $FeCO_3$ crystals due to change in local electrolyte chemistry. The change in local chemistry would lead to a potential shift and the establishment of a galvanic driving force.
- Further propagation of localized corrosion was observed even when a protective $FeCO_3$ layer had formed on the carbon steel surface. Separation of anodes and cathodes within the crevice can take place, either due to difference in local chemistries or due to geometrical configuration of the crevice. The establishment of the local galvanic cells has the potential to lead to further propagation of the localized corrosion.

Data Availability

The raw/processed data required to reproduce these findings cannot be shared at this time as the data also forms part of an ongoing study.

Acknowledgements

The authors would like to acknowledge the funding and technical support from BP International Ltd, United Kingdom, grant reference EP/R00496X/1.

References

1. Fosbøl, P.L., Thomsen, K. and Stenby, E.H. Improving Mechanistic CO_2 Corrosion Models. In: *CORROSION 2009*, *2009/1/1/*, *Atlanta, Georgia*. NACE: NACE International, 2009, p.23.
2. Nešić, S. Key issues related to modelling of internal corrosion of oil and gas pipelines – A review. *Corrosion Science.* 2007, **49**(12), pp.4308-4338.
3. Kermani, M.B. and Morshed, A. Carbon dioxide corrosion in oil and gas production - A compendium. *Corrosion.* 2003, **59**(8), pp.659-683.
4. Frankel, G.S. and Sridhar, N. Understanding localized corrosion. *Materials Today.* 2008, **11**(10), pp.38-44.
5. Ahmad, Z. CHAPTER 4 - TYPES OF CORROSION: Materials and Environments. In: Ahmad, Z. ed. *Principles of Corrosion Engineering and Corrosion Control*. Oxford: Butterworth-Heinemann, 2006, pp.120-270.
6. Barker, R., Yazdi, R., Hua, Y., Jackson, A., Ghanbarzadeh, A., Huggan, M., Charpentier, T. and Neville, A. Development of an automated underwater abrasion rig to determine galvanic effects during the growth and localised breakdown of surface films in CO_2-containing solutions. *Review of Scientific Instruments.* 2019, **90**(3), p.034101.

7. Han, J., Brown, B.N. and Nesic, S. Investigation of the Galvanic Mechanism for Localized Carbon Dioxide Corrosion Propagation Using the Artificial Pit Technique. *Corrosion.* 2010, **66**(9).
8. Hassani, S., Huang, J., Victor, A.C., Brown, B. and Singer, M. Inhibited Under-Deposit CO_2 Corrosion: Small Particle Silica Sand and Eicosane Paraffin Deposits. In: *CORROSION 2017*, *2017/4/27/*, *New Orleans, Louisiana, USA*. NACE: NACE International, 2017, p.12.
9. Huang, J., Brown, B., Nesic, S., Papavinasam, S. and Gould, D. Localized Corrosion of Mild Steel under Silica Deposits in Inhibited Aqueous CO_2 solutions. In: *CORROSION 2013*, *2013/3/17/*, *Orlando, Florida*. NACE: NACE International, 2013, p.17.
10. Huang, J., Brown, B., Jiang, X., Kinsella, B. and Nesic, S. Internal CO_2 Corrosion Of Mild Steel Pipelines Under Inert Solid Deposits. In: *CORROSION 2010*, *2010/1/1/*, *San Antonio, Texas*. NACE: NACE International, 2010, p.18.
11. Kain, R.M. Crevice Corrosion Behavior of Stainless Steel in Seawater and Related Environments. *Corrosion.* 1984, **40**(6), pp.313-321.
12. Pickering, H.W. The significance of the local electrode potential within pits, crevices and cracks. *Corrosion Science.* 1989, **29**(2), pp.325-341.
13. Oldfield, J.W. and Sutton, W.H. Crevice Corrosion of Stainless Steels: I. A Mathematical Model. *British Corrosion Journal.* 1978, **13**(1), pp.13-22.
14. Kain, R.M., Tuthill, A.H. and Hoxie, E.C. The resistance of types 304 and 316 stainless steels to crevice corrosion in natural waters. *Journal of Materials for Energy Systems.* 1984, **5**(4), pp.205-211.
15. Wu, L., Guo, D., Li, M., Joseph, J., J. Noël, J., Keech, P. and Wren, J. Inverse Crevice Corrosion of Carbon Steel: Effect of Solution Volume to Surface Area. *Journal of the Electrochemical Society.* 2017, **164**, pp.C539-C553.
16. Li, Y.Z., Xu, N., Liu, G.R., Guo, X.P. and Zhang, G.A. Crevice corrosion of N80 carbon steel in CO_2-saturated environment containing acetic acid. *Corrosion Science.* 2016, **112**, pp.426-437.
17. Nordsveen, S., Nesic, S., Nybors, R. and A., S. A Mechanistic Model for Carbon Dioxide Corrosion of Mild Steel in the Presence of Protective Iron Carbonate Films—Part 1: Theory and Verification. *Corrosion.* 2003, **59**(5), pp.443-456.
18. Sun, W. and Nesic, S. Kinetics of corrosion layer formation: Part 1 - Iron carbonate layers in carbon dioxide corrosion. *Corrosion.* 2008, **64**(4), pp.334-346.
19. Kahyarian, A., Achour, M. and Nesic, S. CO_2 corrosion of mild steel. In: *Trends in Oil and Gas Corrosion Research and Technologies*. 2017, pp.149-190.
20. Barker, R., Burkle, D., Charpentier, T., Thompson, H. and Neville, A. A review of iron carbonate ($FeCO_3$) formation in the oil and gas industry. *Corrosion Science.* 2018.
21. Burkle, D., De Motte, R., Taleb, W., Kleppe, A., Comyn, T., Vargas, S.M., Neville, A. and Barker, R. In situ SR-XRD study of $FeCO_3$ precipitation kinetics onto carbon steel in CO_2-containing environments: The influence of brine pH. *Electrochimica Acta.* 2017, **255**.
22. De Motte, R., Barker, R., Burkle, D., Vargas, S.M. and Neville, A. The Early Stages of $FeCO_3$ Scale Formation Kinetics in CO_2 Corrosion. *Materials Chemistry and Physics.* 2018, **216**.
23. Hua, Y., Shamsa, A., Barker, R. and Neville, A. Protectiveness, morphology and composition of corrosion products formed on carbon steel in the presence of Cl^- , Ca^{2+} and Mg^{2+} in high pressure CO_2 environments. *Applied Surface Science.* 2018, **455**.
24. Han, J., Young, D., Colijn, H., Tripathi, A. and Nesic, S. Chemistry and Structure of the Passive Film on Mild Steel in CO_2 Corrosion Environments. *Industrial and Engineering Chemistry Research.* 2009, **48**(13), pp.6296-6302.
25. Han, J., Yang, Y., Nesic, S. and Brown, B.N. Roles Of Passivation And Galvanic Effects In Localised CO_2 Corrosion Of Mild Steel. In: *Corrosion 2008 Conference and Expo*, *New Orleans, Louisiana*. Houston, Texas: NACE International, 2008.
26. Pessu, F., Barker, R. and Neville, A. The Influence of pH on Localized Corrosion Behavior of X65 Carbon Steel in CO_2-Saturated Brines. *Corrosion.* 2015, **71**(12), pp.1452-1466.

27. Mohammed, S., Hua, Y., Barker, R. and Neville, A. Investigating pitting in X65 carbon steel using potentiostatic polarisation. *Applied Surface Science.* 2017, **423**, pp.25-32.
28. Han, J. and William Carey, J. Localized CO_2 corrosion propagation at moderate $FeCO_3$ supersaturation initiated by mechanical removal of corrosion scale. *Journal of Applied Electrochemistry.* 2011, **41**(11), p.1367.
29. Papavinasam, S. Chapter 5 - Mechanisms. In: Papavinasam, S. ed. *Corrosion Control in the Oil and Gas Industry*. Boston: Gulf Professional Publishing, 2014, pp.249-300.
30. Scully, J.R. Polarization Resistance Method for Determination of Instantaneous Corrosion Rates. *Corrosion.* 2000, **56**(2), pp.199-218.
31. Burkle, D., De Motte, R., Taleb, W., Kleppe, A., Comyn, T., Vargas, S., Neville, A. and Barker, R. Development of an electrochemically integrated SR-GIXRD flow cell to study $FeCO_3$ formation kinetics. *Review of Scientific Instruments.* 2016, **87**, pp.105125-101804.
32. Nesic, S., Postlethwaite, J. and Olsen, S. An Electrochemical Model for Prediction of Corrosion of Mild Steel in Aqueous Carbon Dioxide Solutions. *Corrosion.* 1996, **52**(4), pp.280-294.
33. ASTM. *Standard Practice for Preparing, Cleaning, and Evaluating Corrosion Test Specimens.* West Conshohocken, PA: ASTM International, 2017.
34. ASTM. *Standard Practice for Microetching Metals and Alloys.* West Conshohocken, PA: ASTM International, 2015.
35. De Motte, R., Basilico, E., Mingant, R., Kittel, J., Ropital, F., Combrade, P., Necib, S., Deydier, V., Crusset, D. and Marcelin, S. A study by electrochemical impedance spectroscopy and surface analysis of corrosion product layers formed during CO_2 corrosion of low alloy steel. *Corrosion Science.* 2020, **172**, p.108666.
36. Farelas, F., Galicia, M., Brown, B., Nesic, S. and Castaneda, H. Evolution of dissolution processes at the interface of carbon steel corroding in a CO_2 environment studied by EIS. *Corrosion Science.* 2010, **52**(2), pp.509-517.
37. Kakooei, S., Ismail, M., Raja, B., Mohebbi, H., Emamian, S. and Moayedfar, M. Formation of Nano-Scale $FeCO_3$ Protective Corrosion Product in Carbon Dioxide-Saturated 3% Sodium Chloride Solution. *Key Engineering Materials.* 2017, **740**, pp.3-8.
38. Pandarinathan, V., Lepková, K. and van Bronswijk, W. Chukanovite ($Fe_2(OH)_2CO_3$) identified as a corrosion product at sand-deposited carbon steel in CO_2-saturated brine. *Corrosion Science.* 2014, **85**, pp.26-32.
39. Azoulay, I., Rémazeilles, C. and Refait, P. Determination of standard Gibbs free energy of formation of chukanovite and Pourbaix diagrams of iron in carbonated media. *Corrosion Science.* 2012, **58**, pp.229-236.
40. Osório, W.R., Peixoto, L.C. and Garcia, A. Electrochemical corrosion behaviour of a Ti-IF steel and a SAE 1020 steel in a 0.5 M NaCl solution. *Materials and Corrosion.* 2010, **61**(5), pp.407-411.
41. Osório, W.R., Peixoto, L.C., Garcia, L.R. and Garcia, A. Electrochemical corrosion response of a low carbon heat treated steel in a NaCl solution. *Materials and Corrosion.* 2009, **60**(10), pp.804-812.
42. Al-Hassan, S., Mishra, B., Olson, D.L. and Salama, M.M. Effect of Microstructure on Corrosion of Steels in Aqueous Solutions Containing Carbon Dioxide. *Corrosion.* 1998, **54**(6), pp.480-491.
43. Hu, Q., Guo, X., Zhang, G. and Zehua, D. The corrosion behavior of carbon steel in CO_2-saturated NaCl crevice solution containing acetic acid. *Materials and Corrosion.* 2011, **63**.
44. Vera, J.R., Daniels, D. and Achour, M.H. Under deposit corrosion (UDC) in the oil and gas industry: A review of mechanisms, testing and mitigation. *NACE - International Corrosion Conference Series.* 2012, **4**, pp.3028-3040.